Journal of Alloys and Compounds 840 (2020) 155669

Contents lists available at ScienceDirect

Journal of Alloys and Compounds

journal homepage: http://www.elsevier.com/locate/jalcom

Influence of gadolinium (Gd^{3+}) ion substitution on structural, magnetic and electrical properties of cobalt ferrites

A.B. Kadam [a], Vishwanath K. Mande [b], S.B. Kadam [c], R.H. Kadam [d], Sagar E. Shirsath [e], Rameshwar B. Borade [f, *]

[a] Department of Physics, Jawahar Art Science and Commerce College, Andur, Osmanabad, 413601, MS, India
[b] Department of Physics, K.K.M. College, Manwath, Parbhani, 431505, MS, India
[c] Department of Physics, L.B.S. College, Partur, Jalna, 431501, MS, India
[d] Materials Science Research Laboratory, Shrikrishna Mahavidyalaya, Gunjoti, Osmanabad, 413613, MS, India
[e] Department of Physics, Vivekanand College, Aurangabad, 431001, MS, India
[f] Department of Physics, MSS's Arts, Science and Commerce College, Ambad, Jalna, 431204, MS, India

ARTICLE INFO

Article history:
Received 12 April 2020
Received in revised form
14 May 2020
Accepted 15 May 2020
Available online 23 May 2020

Keywords:
Gd-substituted Co-ferrite
Structural analysis
Rietveld refinement
Cation distribution
Saturation magnetization
Dielectric constant

ABSTRACT

In present work, $CoFe_{2-x}Gd_xO_4$ nanoparticles with compositions x = 0.0, 0.02, 0.04, 0.06, 0.08 and 0.1 were successfully synthesized by a sol-gel auto-combustion route sintered at 700 °C for 5 h. The effect of Gd^{3+} substitution on structural, morphological, magnetic and dielectric properties has been investigated. The X-ray diffraction with Rietveld refinement reveals that Gd-substituted Co-ferrites are prepared in a single-phase cubic spinel structure. Fourier transform infrared and Raman spectra confirm the single-phase formation of cubic spinel structure. It is observed that the lattice constants decrease from 8.3776 to 8.3711 Å with the substitution of Gd composition from x = 0.0 to 0.1. This is because of the distortion of the lattice structure with the introduction of Gd^{3+} ions. The crystallite size calculated from X-ray diffraction decreases from 29 to 19 nm with Gd^{3+} composition which confirms the formation of nanocrystalline samples. These values are good agreement with crystallite size calculated by the Williamson Hall method. The distribution of cations among the octahedral B and tetrahedral A-site was estimated by the computational method. Field emission scanning electron microscopy (FE-SEM) also confirmed the nanostructural nature in the range of 200–300 nm. Energy dispersive analysis (EDAX) proves chemical purity and stoichiometry. Fourier transform infrared spectra show the main vibration band of spinel structure. Gd-doped Co-ferrite shows the characteristics Raman active modes of spinel structure. Magnetic study reveals that saturation magnetization decreases from 77.37 to 51.38 emu/g with an increase of Gd composition in cobalt ferrites. It is observed that the coercivity of samples is increased from 976 to 1281 Oe with Gd substitution. Dielectric properties measured from LCR-Q meter exhibits the Maxwell–Wagner model.

1. Introduction

The research of the doped ferrites is more attracted in recent years because of their wide applications in various technologies. Spinel ferrites with chemical formula MFe_2O_4 (Where, M = Ni, Co, Zn, etc.) have superior properties like optical, electrical and magnetic, therefore, they are technologically and scientifically important [1,2]. In MFe_2O_4 structure, metal cation M occupies tetrahedral (A) site, Fe occupies octahedral (B) site and oxygen anions form a close-packed face-centered cubic structure [3,4]. Among these ferrites, $CoFe_2O_4$ was widely studied in the last decade due to its properties like high Curie temperature, high electrical resistivity, high coercivity, high mechanical and chemical stability, high magnetocrystalline anisotropy and moderate saturation magnetization [5,6]. These properties give extensive technological applications such as recording media, drug delivery systems, catalysis, sensors, and microwave devices [7–10]. $CoFe_2O_4$ crystallizes in spinel cubic structure with space group Fd-3m in nanoparticles and it crystallizes in inverse spinel in case of bulk samples. In the case of the spinel structure, divalent cobalt ions (Co^{2+}) occupy at both octahedral and tetrahedral sites and its occupancy depends on

* Corresponding author.
E-mail address: rborade1987@gmail.com (R.B. Borade).

https://doi.org/10.1016/j.jallcom.2020.155669
0925-8388/

synthesis technique and conditions. The magnetic parameter depends on super-exchange coupling between different ions occupied at octahedral and tetrahedral sites [11,12].

The physical and chemical properties of cobalt ferrites can be tuned by substituting different cations at the tetrahedral or octahedral sites. There are so many works of literature are available on the substitution effect of divalent, trivalent and tetravalent ions other than rare earth on cobalt ferrites [13–15]. The structural disorder, lattice strain and other properties of cobalt ferrite can be altered by the substitution of rare earth (RE) metal ions like Gd^{3+}, Nd^{3+}, Sm^{3+}, Ho^{3+}, and Y^{3+}, etc. Introduction of rare earth (RE) metal ions into the cobalt ferrites give excellent magnetic properties which are suitable for memory storage devices and recording media. Rare-earth element has 4f unpaired electrons and iron has 3 d unpaired electrons, therefore, the substitution of RE^{3+} induces RE^{3+}-Fe^{3+} interaction which turns out the magnetic, structural, spectral and electrical properties. Moreover, the nature of cation distribution, morphology of particles, ionic size, chemical compositions and preparation methods affect the properties of cobalt ferrite. There are several number of chemical and physical techniques developed for the preparation of ferrites e.g., sol–gel method, ball milling, hydrothermal, ceramic method, organic precursor and co-precipitation method, etc. [2,16–18]. In the last decade, the sol-gel auto-combustion technique is extensively used for the preparation of all types of ferrites because reagents are mixed at the molecular level and therefore there is good control of stoichiometry, purity, homogeneity, and morphology. Besides, this method is simple, low cost and required low sintering temperature for the final product of ferrite samples as compared to other methods [19].

Literatures on the substitution effect of RE trivalent ion on the properties of cobalt ferrites are available. Manisha Dhiman et al. synthesized RE (RE = Eu, Gd, and Dy) substituted cobalt ferrites and observed that saturation magnetization decreases with the substitution of RE^{3+} ions in cobalt ferrites [20]. C. Murugesan et al. prepared Gd-substituted cobalt ferrite and reported that dielectric constant increases with introducing Gd [21]. F.R. Mariosi et al. developed a series on La-substituted cobalt ferrite and found that lattice constant increases with an increase in lanthanum substitution. They also observed from Raman spectra, that the crystalline structure shows a significant effect of lanthanum substitution [22].

By inspiring from these works, we have been synthesized a series $CoFe_{2-x}Gd_xO_4$ (x = 0.0, 0.02, 0.04, 0.06, 0.08 and 0.1) by sol-gel auto-combustion technique. Therefore, in this work, we reported the structural, morphological, dielectric and magnetic properties of Gd-substituted cobalt ferrites for better understanding and desired applications.

2. Experimental procedure

2.1. Sample preparation

The nanocrystalline samples of $CoFe_{2-x}Gd_xO_4$ (x = 0.0, 0.02, 0.04, 0.06, 0.08 and 0.1) for all the composition have been synthesized via sol-gel auto-combustion technique. The A.R. grade cobalt nitrate [$Co(NO_3)_2 \cdot 6H_2O$] (Sigma-Aldrich, 99.9%), ferric nitrate [$Fe(NO_3)_3 \cdot 9H_2O$] (Acros, 99.9%), gadolinium nitrate [$Gd(NO_3)_3 \cdot 6H_2O$] and citric acid monohydrate (Acros, 99.9%) as a chelating agent were used for the synthesis of $CoFe_{2-x}Gd_xO_4$ (x = 0.0, 0.02, 0.04, 0.06, 0.08 and 0.1) material. The liquid ammonia (NH_3) is used to maintain the pH value of precursor solutions.

The required amount of the starting materials; nitrates and citric acid were dissolved separately in different beakers in few amounts of distilled water. The molar ratio of metal nitrate to citric acid was taken as 1:3. The separate dissolution of the starting material was completed in 2 h. All these solutions were mixed in a beaker after complete dissolution in separate beakers. This solution was continuously mixed by the magnetic stirrer and placed on the hot plate having a temperature of 90 °C for the evaporation up to the gel formation. Once the gel is formed, these were dried at about 250 °C for the combustion of gel and converted into ash. The brown colored powder was formed after the auto-combustion process known as a precursor. The end products of all the composition of this series were prepared in a similar manner. 1 g sample powder was pressed uniaxial to obtain pellets of dimension 3 × 10 mm in a hydraulic machine by applying 5-ton pressure. All the sample powders and pellets were annealed at 700 °C for 5 h to obtain the final product of nanocrystalline $CoFe_{2-x}Gd_xO_4$ (x = 0.0, 0.02, 0.04, 0.06, 0.08 and 0.1) spinel ferrites. The reaction of formation of Gd-substituted cobalt ferrite from the starting materials is as follow,

$$Co(NO_3)_2 \cdot 6H_2O + (2\text{-}x)Fe(NO_3)_3 \cdot 9H_2O + x\,Gd(NO_3)_3 \cdot 6H_2O + 8C_6H_8O_7 \cdot H_2O \rightarrow CoFe_{2-x}Gd_xO_4 + HNO_3\uparrow + H_2O\uparrow + CO_2\uparrow \quad (1)$$

2.2. Characterization

To identify the phase and microstructure of the samples, XRD pattern was recorded with the help of X-rays (λ = 0.154 nm) by Bruker X-ray diffractometer within the range of diffracting angle 10–80°. Rietveld refinement of XRD data was carried out by the Full-prof program by calibrating different parameters. FE-SEM (MIRA-3 LMH, JEOL JSM-6360) was used to study morphology, grain size, and shape of the prepared samples. The stoichiometry and elemental composition of optimized samples were determined by EDAX (INCA Oxford, attached to the FE-SEM). Vibrating sample magnetometer (VSM) was used to record the hysteresis loops and study the magnetic properties at 2 T. Dielectric properties were studied with the help of LCR-Q meter.

3. Result and discussion

3.1. Structural analysis

The XRD pattern for all the samples of a series; $CoFe_{2-x}Gd_xO_4$ (x = 0.0, 0.02, 0.04, 0.06, 0.08 and 0.1) are shown in Fig. 1. Pattern reveled that all the samples crystallize in spinel cubic structure with space group Fd-3m. All the reflection planes observed in XRD patterns; (1 1 1); (2 2 0); (3 1 1); (2 2 2); (4 0 0); (4 2 2); (5 1 1); (4 4 0); (6 2 0); (5 3 3) and (6 2 2) are well matched with standard $CoFe_2O_4$ (JCPDS no.: 03–0864). The XRD pattern does not show any impurity phases in the prepared samples of Gd-substituted Co-ferrite. This ensures that prepared samples are formed in single phase and Gd comprehensively dissolved in the Co-ferrite.

Values of the lattice parameter (a) were calculated by the combination of interplanar spacing (d) and reflection planes (h k l) using the following equation [23]:

$$a = \sqrt{\frac{\lambda^2}{4\sin^2\theta}\left(h^2 + k^2 + l^2\right)} \quad (2)$$

The calculated values of lattice parameters with Gd composition are listed in Table 1. The value of lattice constant for pure $CoFe_2O_4$ is 8.3776 Å which is similar to previous literature [24]. The effective ionic radii are related to the coordination number and the coordination number of the cations at B-site of spinel ferrite is 6 [25]. The effective ionic radii of Gd^{3+} and Fe^{3+} ions with coordination number 6 are 0.938 Å and 0.645 Å respectively [26]. In this series, smaller Fe^{3+} ions are replaced by larger Gd^{3+} ions and therefore, it

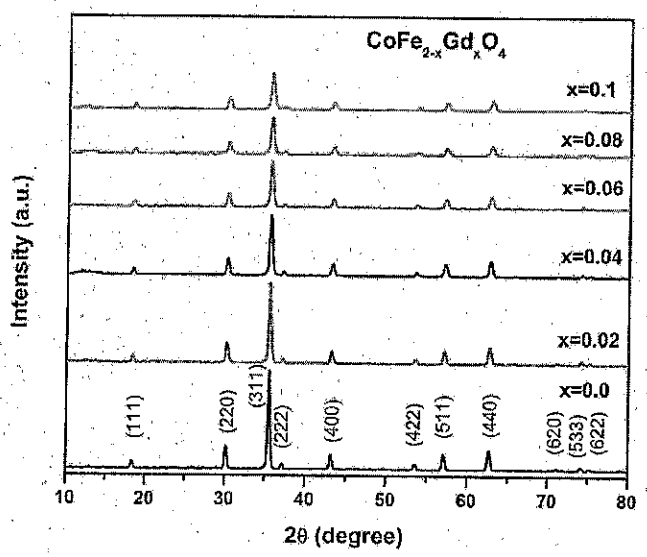

Fig. 1. XRD pattern of $CoFe_{2-x}Gd_xO_4$ (x = 0.0, 0.02, 0.04, 0.06, 0.08 and 0.1) nanoparticles.

is expected to increase lattice constant with the substitution of Gd composition. From Fig. 2 (a), it is observed that the lattice constants decrease from 8.3776 to 8.3711 Å with the substitution of Gd composition from x = 0.0 to 0.1. Larger size gadolinium substitution will distort lattice of Co-ferrites which decrease the lattice constant. The decreasing trend of lattice constant with the substitution of Gd^{3+} ions in Co-ferrites is also observed in previous literature by R.S. Yadav and et al. [27].

From most the intense peak (311) of the XRD pattern, the crystallite sizes of the Gd-substituted Co-ferrites were determined by the Debye-Scherer equation [28].

$$D = \frac{K\lambda}{\beta \cos\theta} \tag{3}$$

Where λ is a wavelength of incident X-ray, β is full width at half maximum intensity, and K is a shape factor that has value 0.9. The variation of the crystallite size of Co-ferrite with Gd composition is shown in Fig. 2 (a). It is observed that crystallite size decreases from 29.43 to 18.60 nm when Gd concentration increases from x = 0.0 to x = 0.1. This range (29–19 nm) of the crystallite size of synthesized samples ensures that the Gd-substituted sample formed in nano-crystalline nature. Values of X-ray density were determined by the equation: $d_x = \frac{8M}{N_A V}$ [29], where M is the molecular weight of the respective composition, N_A is the Avogadro's number and V is unit cell volume. The values of Bulk density (d_B) were estimated by the Archimedes principle [30]. Variation of X-ray density and bulk density with Gd composition are shown in Fig. 2 (b), which exhibits that both X-ray and bulk densities are directly proportional to the concentration of Gd in Co-ferrites. Since X-ray density depends on the molecular weight of respective sample and molecular weight of $CoFe_{2-x}Gd_xO_4$ (x = 0.0, 0.02, 0.04, 0.06, 0.08 and 0.1) are observed to increase from 234.62 g/mol to 244.76 g/mol. Hence, the values of the 'dx' increase with the increasing Gd concentration in Co-ferrites.

The percentage porosity of the prepared sample was calculated with the help of bulk density and X-ray density by the equation [31]:

$$P = 1 - \frac{d_B}{d_x}\% \tag{4}$$

The estimated values of percentage porosity are tabulated in Table 1. It is observed that percentage porosity decreases with the substitution of Gd in Co-ferrites. This is due to the increase in X-ray density because porosity is inversely proportional to the X-ray density.

Table 1
Lattice parameter (a), crystallite size (d_{xrd}), X-ray density (d_x), bulk density (d_B) and porosity (P) of $CoFe_{2-x}Gd_xO_4$ (x = 0.0, 0.02, 0.04, 0.06, 0.08 and 0.1) nanoparticles.

Composition (x)	a (Å)	d_{xrd} (nm)	d_x (g cm^{-3})	d_B (g cm^{-3})	P (%)
0.0	8.3776	29.43	5.300	2.947	44.41
0.02	8.3749	26.46	5.352	3.014	43.68
0.04	8.3742	21.97	5.399	3.057	43.37
0.06	8.3739	20.16	5.446	3.096	43.15
0.08	8.3727	18.80	5.494	3.235	41.12
0.1	8.3711	18.60	5.543	3.285	40.73

3.1.1. Rietveld refinement

The XRD pattern (black solid circles), Rietveld refinement (red solid lines), Bragg positions (bars) and, the difference between observed and calculated data (bottom) of Gd-substituted Co-ferrites are shown in Fig. 3. The peaks observed in the pattern are well indexed according to PDF 22–1086 which confirming the formation of a cubic spinel-type structure with space group Fd-3m. The absence of any extra peak in the pattern exhibit the formation of single-phase Gd-substituted Co-ferrite and incorporation of Gd in $CoFe_2O_4$ lattice. The Rietveld refinement parameters like expected R factor (R_{exp}), weighted profile R-factor (R_{wp}), goodness of fit (χ^2) and, lattice constants are tabulated in Table 2. The fitting of observed XRD data is investigated by goodness of fit (χ^2) and low values of χ^2 confirm the goodness of refinement. It is noticed that lattice constant decreases from 8.3805 to 8.3724 Å with Gd composition in Co-ferrite from x = 0.0 to 0.1. It is expected that lattice constant should be increased because of the difference between the ionic radii of Gd^{3+} (0.938 Å) and Fe^{3+} (0.645 Å) but lattice $CoFe_2O_4$ is distorted with Gd composition. Also, due to the presence of point defects or vacancies of Fe^{3+} ions in the samples during sintering and synthesis decrease the lattice constants. Therefore, the lattice constant is decreased with Gd composition in cobalt ferrite. Similar decreasing trends of lattice constant are reported in the literature [32]. The variations of the peak position with 2θ are shown in Fig. 4. It is found that position of peak (311) is slightly shifted towards a higher angle with Gd composition in cobalt ferrites which indicates the lattice distortion due to the introduction of Gd^{3+} ions in Co-ferrites. This distortion in the lattice is responsible for the discrepancy of ionic radii of host and substituted ions.

Bond lengths and bond angles have been determined with the help of the EXPGUI program using Rietveld refined parameters [33]. Distances from O anions to cations at the (A) and [B] sites (d_{AO} and d_{BO}), and distance from the cations at the (A) sites to those at the [B] sites (d_{AB}) are listed in Table 2. It is observed that d_{AO} bond length increased whereas the d_{BO} bond angle decreased by small margin with Gd^{3+} ions in Co-ferrite. This indicates that tetrahedra are expanding with maintaining their original symmetry [2,3]. $\angle_{O-A-O}$ is angle between anion and cation at A-site, $\angle_{O-B-O}$ is angle between anion and cation at B-site, $\angle_{A-O-B}$ is angle between anion and cations at A and B-site varied with the substation of Gd ions. This is attributed to the change in distribution of cations in A and B-site [34].

3.1.2. Williamson-Hall analysis

To study geometric properties of prepared samples, strain induced in the samples and their crystallite sizes were determined

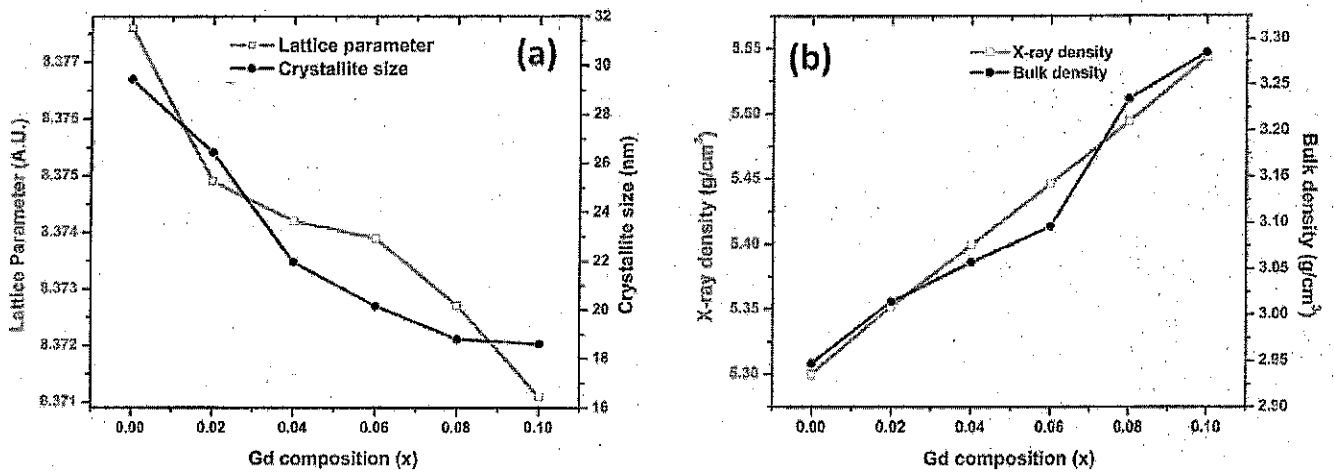

Fig. 2. (a) Variation of lattice parameters and crystallite size (b) variation of X-ray density and bulk density with Gd composition.

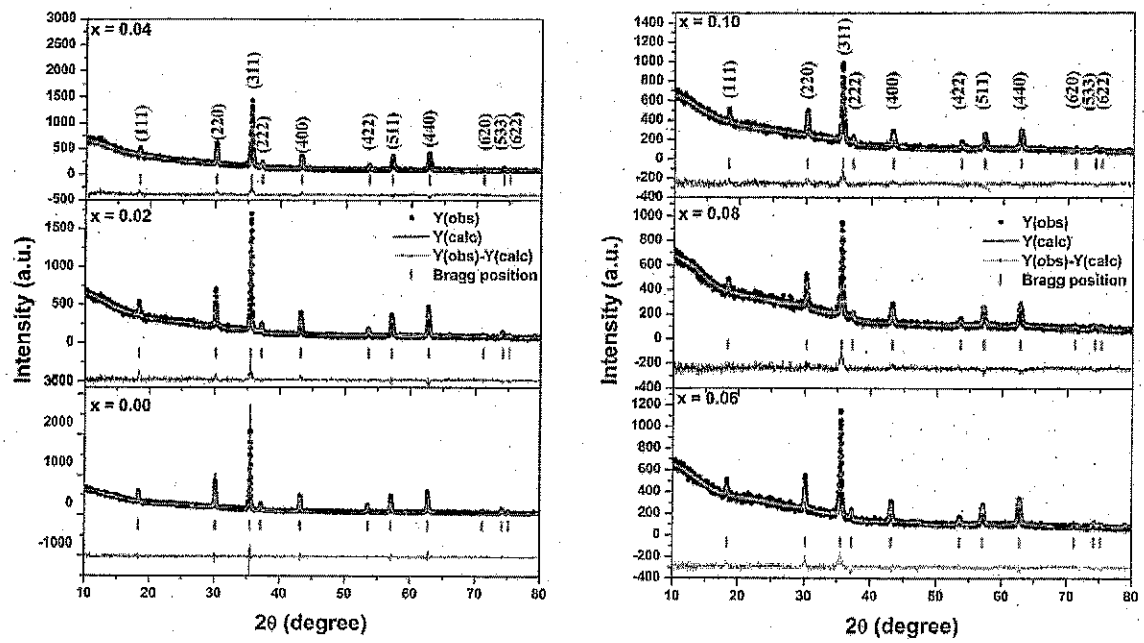

Fig. 3. Rietveld refined XRD patterns of $CoFe_{2-x}Gd_xO_4$ (x = 0.0, 0.02, 0.04, 0.06, 0.08 and 0.1) nanoparticles.

Table 2
Structural parameters obtained from Rietveld Refinement. a_{Riet} lattice constant obtained by Rietveld method, R_{exp} is expected values, Rwp is discrepancy factor, $\chi 2$ is goodness fit, and d_{AO} is distances from the O anion to the cations at the tetrahedral (A)-site, d_{BO} distances from the O anion to the cations at the octahedral-(B) site, d_{AB} is the distance from the cations at the (A) sites to those at the [B] sites, $\angle_{o\text{-}A\text{-}O}$ is angle between anion and cation at A-site, $\angle_{o\text{-}B\text{-}O}$ is angle between anion and cation at B-site, $\angle_{A\text{-}O\text{-}B}$ is angle between anion and cations at A and B-site, t_{UDM} is the crystallite size and ϵ is strain obtained from the Williamson-Hall - uniform deformation model.

Composition (x)	a_{Riet} (Å)	R_{exp}	R_{wp}	χ^2	d_{AO} (Å)	d_{BO} (Å)	d_{AB} (Å)	$\angle_{o\text{-}A\text{-}O}$ (°)	$\angle_{o\text{-}A\text{-}O}$ (°)	$\angle_{A\text{-}O\text{-}B}$ (°)	t_{UDM} (nm)	$\epsilon \times 10^{-4}$
0.0	8.3805	7.18	8.18	1.29	1.9959	1.9959	3.4744	109.47	91.95	123.89	29.00	7.52
0.02	8.3775	7.17	8.13	1.29	2.0111	1.9870	3.4731	109.47	88.61	126.26	25.25	5.68
0.04	8.3768	7.15	7.98	1.25	2.0124	1.9861	3.4728	109.47	88.93	124.35	22.29	4.99
0.06	8.3759	7.00	7.87	1.26	2.0136	1.9851	3.4725	109.47	86.92	127.47	21.36	3.98
0.08	8.3731	6.90	7.20	1.09	2.0130	1.9845	3.4713	109.47	93.17	122.11	19.86	2.68
0.10	8.3724	6.99	7.48	1.14	2.0142	1.9836	3.4710	109.47	93.51	121.76	19.02	2.06

with the help of Williamson-Hall assuming uniform deformation model (UDM). The strain induced in prepared samples during synthesis and sintering process is determined by the relation [35].

$$\varepsilon = \frac{\beta}{4\tan\theta} \tag{5}$$

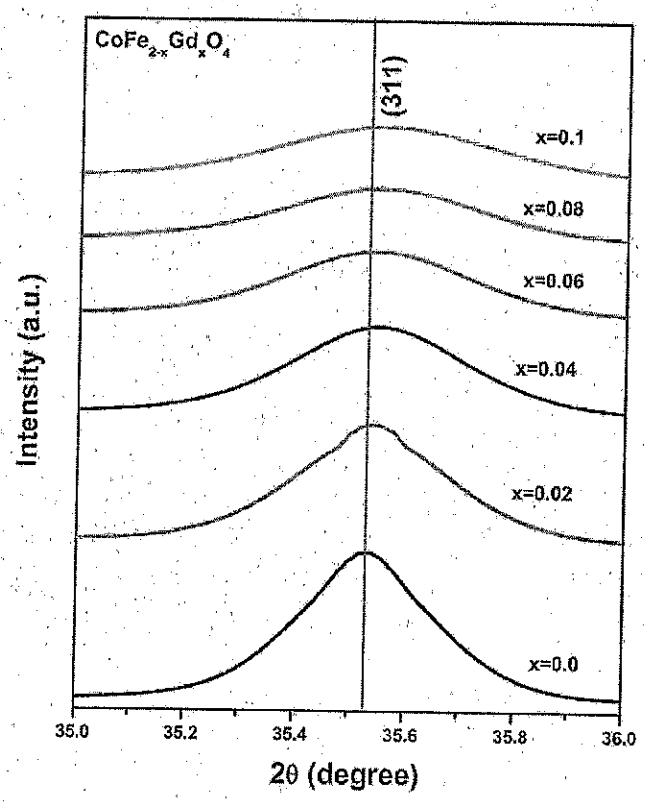

Fig. 4. Enlarged view of XRD pattern of $CoFe_{2-x}Gd_xO_4$ (x = 0.0, 0.02, 0.04, 0.06, 0.08 and 0.1) nanoparticles.

The total broadening of the peak is a combined effect of broadening due to strain and broadening due to crystallite size,

$$\beta = \beta_\varepsilon + \beta_D \tag{6}$$

From equations (3), (5) and (6)

$$\beta = 4\varepsilon \tan\theta + \frac{K\lambda}{D\cos\theta} \tag{7}$$

Rewriting above equation

$$\beta\cos\theta = 4\varepsilon\sin\theta + \frac{K\lambda}{D} \tag{8}$$

The graph (Fig. 5) of 4sinθ (on X-axis) versus βcosθ (on Y-axis) was plotted to determine strain induced in the samples and its crystallite size. The slope of the line of fit indicates the strain whereas y-intercept of that line of fit gives the crystallite size of the sample. For all the samples of the Gd-substituted cobalt ferrite have positive slopes which exhibit that tensile strain induced in the samples. The values of crystallite size and strain which extracted from the line fit are shown in Table 2. The values of crystallite size and lattice strain are decreased with increasing of Gd^{3+} ions in Co-ferrite. The substitution of larger ionic radius Gd^{3+} (0.938 Å) ions in place of smaller ionic radius Fe^{3+} (0.645 Å) ions produces strain which prevents the crystal growth. Also, it is noticed that the width of the peak increases with the substitution of Gd which exhibits the decrease of crystallinity of the sample. Since rare earth metal ion Gd^{3+} ions preferred to occupy at octahedral sites because of its larger size. Because of the larger size of Gd^{3+} ion, bond enthalpy of $Gd^{3+}-O^{2-}$ is larger than the bond enthalpy of $Fe^{3+}-O^{2-}$. Therefore, more energy is required for Gd^{3+} ion to occupy at the octahedral site. This change in enthalpy is responsible for the decrease of crystallization and therefore, crystallite size as well as lattice constant decreases with Gd composition. Furthermore, Gd^{3+} ions reside at grain boundary due to the partial substitution which also lowers the crystallization. The values of crystallite size are lying within the range of 29–19 nm which reflects the nanocrystalline nature of the prepared samples. The value of lattice strain is decreased from 7.52 to 2.06 with Gd composition from x = 0.0 to x = 0.1 in Co-ferrite. The strain produced in samples is directly proportional to the lattice constant of the samples [36]. This change in tensile strain gives the evidence of a decrease of lattice constant with Gd composition in Co-ferrites.

3.1.3. Cation distribution

Bertaut method was used to determine the cation distribution at octahedral [B] and tetrahedral (A) sites from XRD data [37]. In this method calculated relative intensity of selected planes was compared with observed relative intensity. The planes were selected by using the relation,

$$\frac{I^{Obs.}_{hkl}}{I^{Obs.}_{h'k'l'}} = \frac{I^{Cal.}_{hkl}}{I^{Cal.}_{h'k'l'}} \tag{9}$$

where, $I^{Calc.}_{hkl}$ and $I^{Obs.}_{hkl}$ are the calculated and observed intensities for planes (hkl) respectively. The planes of the XRD pattern are selected in such a way that the intensity of planes should i) nearly independent on parameters of oxygen ii) change with substitution of the cation in opposite manner iii) not differ significantly [38]. In this paper, planes (220), (422) and (400) were selected to compare the intensity ratio $I_{(220)}/I_{(400)}$ and $I_{(422)}/I_{(400)}$. These planes are presumed to sensitive for the distribution of cation. In this study, absorption and temperature factor are not considered in the calculation because of intensity independent on these factors [39]. The planes of the XRD pattern were selected according to the relation called agreement factor (R).

$$R = \left| \frac{I^{Obs.}_{hkl}}{I^{Obs.}_{h'k'l'}} - \frac{I^{Cal.}_{hkl}}{I^{Cal.}_{h'k'l'}} \right| \tag{10}$$

The value of the agreement (R) factor should be minimum as possible. The intensity of these planes does not depend on the parameters of oxygen. The intensity of planes has been determined by the following equation suggested by Buerger [40].

$$I_{hkl} = |F|^2_{hkl} P \cdot L_P \tag{11}$$

Where L_P is the Lorentz polarization factor, P is the multiplicity factor and F is the structure factor. The structure factors of the required planes are calculated by using the relations [41].

$$F_{220} = 8F_a \tag{12}$$

$$F_{422} = 8F_a \tag{13}$$

$$F_{220} = 8(F_a - 2F_b - 4F_o) \tag{14}$$

where F_a = concentration of A-site cation × atomic scattering factor (f_a), F_b = concentration of B-site cation × atomic scattering factor (f_b) and F_O = atomic scattering factor of oxygen (f_O).

The values of atomic scattering factors f_a, f_b and f_o, multiplicity factors (P) and Lorentz polarization factors (L_P) of corresponding ions or atoms were taken from the literature [41]. Since the relative intensity of the plane in the XRD pattern is determined by the position of cation in a unit cell. Therefore, positions of the cations in

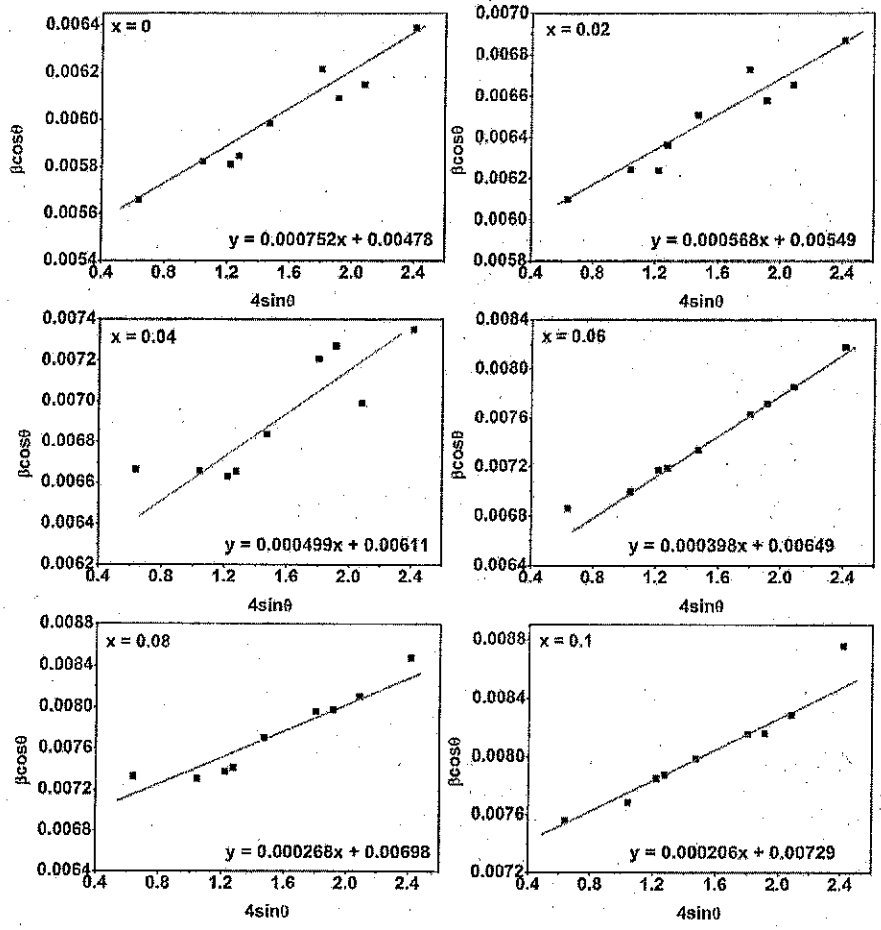

Fig. 5. UDM plot for $CoFe_{2-x}Gd_xO_4$ (x = 0.0, 0.02, 0.04, 0.06, 0.08 and 0.1) nanoparticles.

the unit cell are generally determined by trial and error process because there is no method to determine the position of cation from intensity directly. All the values of required planes were substituted in equation (11) and intensities of those planes were calculated by assuming some fraction of cations at A and B-site. The calculated relative intensities were compared with observed relative intensities. This process was repeated by varying the concentration of cations at A and B-site until the agreement factor becomes minimum.

The estimated cation distribution, intensity ratios and agreement factors are listed in Table 3. It is noted that Co^{2+} and Fe^{3+} ions are preferred to occupy both at octahedral B-site (with 67%) and tetrahedral A-site (with 33%) for pure cobalt ferrite sample. The substitution of Gd^{3+} ions in cobalt ferrite is strongly preferred to occupy at octahedral B-site only. It is known that the size of the octahedral B-site is larger than the size of the tetrahedral A-site which results in larger radius Gd^{3+} ions occupy only at octahedral B-site. It is observed that Co^{2+} ions are transferred from octahedral B-site to tetrahedral A-site with the substitution of Gd^{3+} ions by redistributing the cations among the octahedral and tetrahedral site [42]. It is found that the occupancy of Co^{2+} ions increases and Fe^{3+} ions decreases at the tetrahedral site with substitution of Gd composition in cobalt ferrites. This result is similar to other results reported by the researcher [43,44].

In order to see more insight on structure of unit cell, ionic radii of octahedral site (r_B) and tetrahedral site (r_A) were calculated from the relations [45],

$$r_A = \left[f_c\left(Co^{2+}\right) . r\left(Co^{2+}\right) + f_c\left(Fe^{3+}\right) . r\left(Fe^{3+}\right)\right] \text{ Å} \quad (15)$$

$$r_B = \frac{1}{2}\left[f_c\left(Co^{2+}\right) . r\left(Co^{2+}\right) + f_c\left(Fe^{3+}\right) . r\left(Fe^{3+}\right) + f_c\left(Gd^{3+}\right) . r\left(Gd^{3+}\right)\right] \text{ Å} \quad (16)$$

Where f_c is concentration of cations $r(Co^{2+}) = 0.745$ Å, $r(Fe^{3+}) = 0.645$ Å, $r(Gd^{3+}) = 0.938$ Å. The values of r_A and r_B calculated from above equations are tabulated in Table 4. It is found that ionic radius of tetrahedral site increases with Gd^{3+} ions in cobalt ferrite. This increment of ionic radius is due to the transformation of Co^{2+} ions from B to A-site. The values of ionic radius of octahedral site is decreased for x = 0.02, after that it is increased with Gd composition. This increment of ionic radius is due to larger size Gd3+ ion substituted in place of smaller Fe^{3+} ions.

The anion parameter or oxygen positional parameter (u) can be calculated using the above discussed data by the equation [46]:

$$u = (r_A + R_0)\frac{1}{a\sqrt{3}} + \frac{1}{4} \quad (17)$$

It is assumed that O^{2-} ions are situated at faces of a unit cell with the center of the symmetry $\left(\frac{3}{8}\ \frac{3}{8}\ \frac{3}{8}\right)$ and origin at A-site. From this

Table 3
Cation distribution and intensity ratio calculations for $CoFe_{2-x}Gd_xO_4$ (x = 0.0, 0.02, 0.04, 0.06, 0.08 and 0.1).

Composition (x)	Cation Distribution		Intensity ratios				Agreement Factor	
	A-site	B-site	(220/400)		(422/400)		(220/400)	(422/400)
			Obs.	Cal.	Obs.	Cal.		
0.0	$(Co_{0.33}Fe_{0.67})$	$[Co_{0.67}Fe_{1.33}]$	1.6276	1.4081	0.4598	0.4778	0.2195	−0.0180
0.02	$(Co_{0.6}Fe_{0.4})$	$[Co_{0.4}Fe_{1.58}Gd_{0.02}]$	1.7466	1.4301	0.4907	0.4864	0.3165	0.0043
0.04	$(Co_{0.63}Fe_{0.37})$	$[Co_{0.37}Fe_{1.59}Gd_{0.04}]$	1.7271	1.3907	0.5340	0.4732	0.3364	0.0608
0.06	$(Co_{0.65}Fe_{0.35})$	$[Co_{0.35}Fe_{1.59}Gd_{0.06}]$	1.6633	1.3506	0.5297	0.4596	0.3127	0.0701
0.08	$(Co_{0.67}Fe_{0.33})$	$[Co_{0.33}Fe_{1.59}Gd_{0.08}]$	1.9119	1.3123	0.6153	0.4466	0.5996	0.1687
0.10	$(Co_{0.7}Fe_{0.3})$	$[Co_{0.3}Fe_{1.6}Gd_{0.1}]$	1.6724	1.2779	0.5582	0.4350	0.3945	0.1232

Table 4
Values ionic radii (r_A and r_B) radii of tetrahedral-A and octahedral-B site of Oxygen parameter 'u' and jump length (L_A and L_B) for $CoFe_{2-x}Gd_xO_4$ (x = 0.0, 0.02, 0.04, 0.06, 0.08 and 0.1).

Composition	r_A (Å)	r_B (Å)	u (Å)	L_A (Å)	L_B (Å)
0.0	0.6814	0.6818	0.3875	3.628	2.963
0.02	0.7070	0.6719	0.3886	3.627	2.962
0.04	0.7099	0.6734	0.3887	3.626	2.961
0.06	0.7118	0.6753	0.3888	3.626	2.961
0.08	0.7137	0.6773	0.3888	3.626	2.960
0.10	0.7165	0.6788	0.3889	3.625	2.960

data, it is clear that anion parameter; $u = \frac{3}{8} = 0.375$ for ideal FCC structure of a unit cell. But it is observed that (Table 4) this anion parameter is slightly larger than the ideal in case Gd-substituted Co-ferrites. This deviation indicates the distortion of lattice due to oxygen ions to accommodate the cations at A and B-sites. The values of anion parameter are listed in Table 4. The values of anion parameter are slightly increased with the Gd^{3+} ions in Co-ferrite.

The jump lengths; L_A and L_B between the ions at A and B-site were calculated by the relations [47],

$$L_A = \frac{a\sqrt{3}}{4} \tag{18}$$

$$L_A = \frac{a\sqrt{2}}{4} \tag{19}$$

The values of jump lengths L_A and L_B are tabulated in Table 4. It is observed that both L_A and L_B decreases very slightly with Gd composition in Co-ferrite. This is due to the lattice constant decreases with Gd composition.

3.2. FE-SEM and EDS analysis

To see the morphology of prepared samples, FE-SEM images were taken out for selected samples. Fig. 6 shows the FE-SEM photograph of $CoFe_2O_4$, $CoFe_{1.94}Gd_{0.06}O_4$, and $CoFe_{1.9}Gd_{0.1}O_4$ samples. The range of grain size observed from FE-SEM images is within 200–300 nm. It is found that most of the grains are spherical in shape but they are agglomerated due to the magnetic interaction between the grains. This agglomeration gives evidence of high reactivity and solubility of composition. The degree of agglomeration is decreased with the substitution of Gd in Co-ferrites and it might be due to the decrease in magnetic interaction. It is also observed that the substitution of Gd affects the size of grains. Grain size collectively depends on various factors like sintering temperature, porosity and grain boundary [48]. Grain size decreases with increasing the Gd composition and this may be due to the density of sample increases with Gd composition.

The elemental composition and their proportion of the selected samples of Gd-doped Co-ferrites (x = 0.0, x = 0.06 and x = 0.1) has been confirmed by energy dispersive analysis (EDAX) with the help of FE-SEM and spectra are shown in Fig. 7. EDAX spectra show peaks of the elements; Co, Fe, O, Gd and no impurity peak in it which is the proof of formation pure phase of Gd-doped Co-ferrites. The compositional percentages of Co, Fe, O and Gd in the sample were studied by EDAX spectra and it is found that all elements are in good stoichiometric proportions with an error of 2–3%.

3.3. FT-IR studies

The FT-IR transmittance spectra of $CoFe_{2-x}Gd_xO_4$ (x = 0.0, 0.02, 0.04, 0.06, 0.08 and 0.1) nanopowder measured at room temperature are shown in Fig. 8. FT-IR transmittance spectra show one broad band around 547 cm^{-1} wavenumber. This band is attributed to the vibration of metal-oxygen (Fe–O) bonds at the tetrahedral site. This band in all the composition of Gd in Co-ferrites indicates the formation of spinel ferrite structure. The band observed around 547 cm^{-1} for x = 0.0 is slightly shifted towards the higher wavenumber which assigned to perturbation occurring between metal-oxygen bond due to the substitution of Gd in Co-ferrite. One another band is observed around 2361 cm^{-1} for all the composition of Gd and this band is attributed to aromatic and aliphatic C–H stretching bond [31]. These results are consistent with the XRD result that showed a structural transition with the substitution of Gd in Co-ferrite.

3.4. Raman analysis

Raman analysis is used to study lattice distortion, magnetic ordering, and structure transition in the ferrites nanoparticles. Room temperature measured Raman spectra of Gd-substituted Co-ferrite samples are shown in Fig. 9. According to group theory, spinel structure has 39 normal mode of vibration [21], out of which, A_{1g} (1) (675-688 cm^{-1}), A_{1g} (2) (647-649 cm^{-1}), T_{2g} (1) (516-522 cm^{-1}) and T_{2g} (2) (476-481 cm^{-1}) are shown in Fig. 9. We have observed singly degenerate symmetric mode A_{1g} (1) around 675 cm^{-1} and this band is due to the symmetric stretching vibration bond at the tetrahedral (A) site while A_{1g} (2) around 647 cm^{-1} is related to Co–O bonds. The mode T_{2g} (1) at 516 cm^{-1} is associated with an anti-symmetric bending of oxygen of Fe–O bond whereas; T_{2g} (2) around 476 cm^{-1} is related to asymmetric stretching of oxygen of Co/Gd/Fe–O [32]. The presence of these bands is associated with the spinel structure of ferrite and which also confirms the formation of single-phase Gd-substituted Co-ferrite. The positions of bands observed from the Raman spectra are given in Table 5. From Fig. 9 and Table 5, it is observed that most of the peaks are slightly shifting towards the higher wavenumber with Gd composition. This behavior shows that the substitution of Gd will distort the lattice due to the migration of cations among tetrahedral

Fig. 6. FE-SEM images of $CoFe_{2-x}Gd_xO_4$ (x = 0.0, 0.06 and 0.1) nanoparticles.

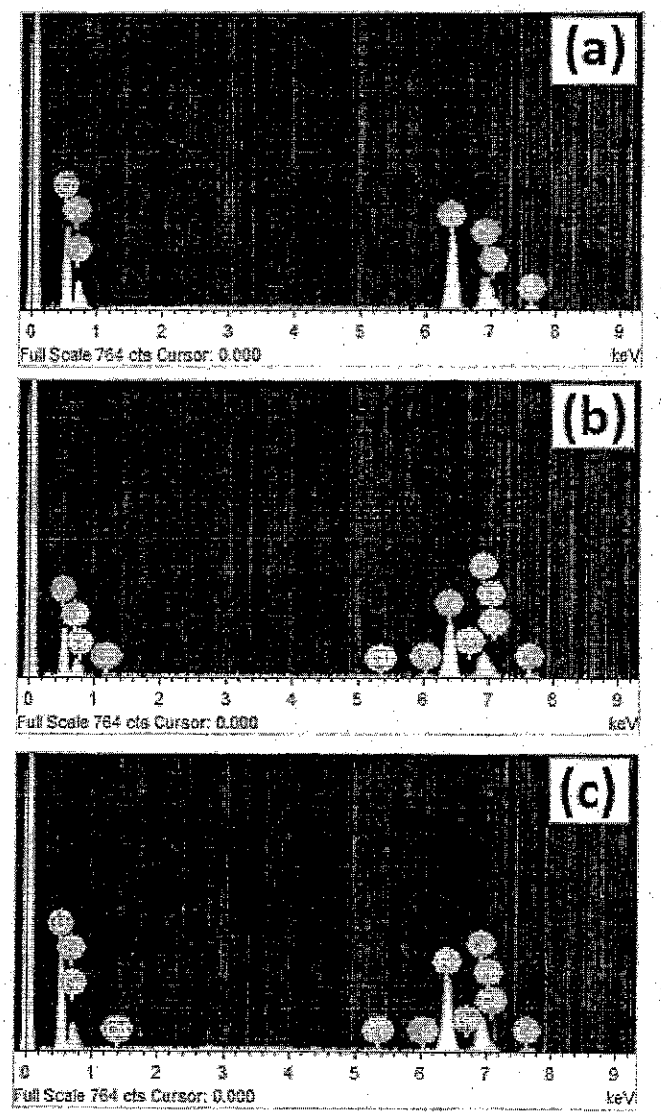

Fig. 7. Energy dispersive X-ray spectroscopy spectra of $CoFe_{2-x}Gd_xO_4$ (x = 0.0, 0.06 and 0.1) nanoparticles.

and octahedral sites. This result confirms the complete incorporation Gd^{3+} in Co-ferrite and it is consistent with the result explained in the XRD analysis with cation distribution.

3.5. Magnetic properties

The VSM was used to study the magnetic properties of $CoFe_{2-x}Gd_xO_4$ (x = 0.0, 0.02, 0.04, 0.06, 0.08 and 0.1) samples by applying the magnetic field up to 1.5 T. The hysteresis loops of all the samples are shown in Fig. 10. It is observed from the hysteresis loop; all samples have moderate soft ferromagnetic nature. The values of saturation magnetization (Ms), coercivity (Hc) and remanence magnetization (Mr) determined from the hysteresis loop are shown in Table 6. Variation of saturation magnetization and coercivity of the samples with Gd composition are shown in Fig. 11. Values of saturation magnetization are decreased from 77.37 to 51.38 emu/g with an increase of Gd composition in cobalt ferrites. Spinel ferrite consists of three super-exchange interactions; A-B interaction, A-A interaction and B–B interaction and among

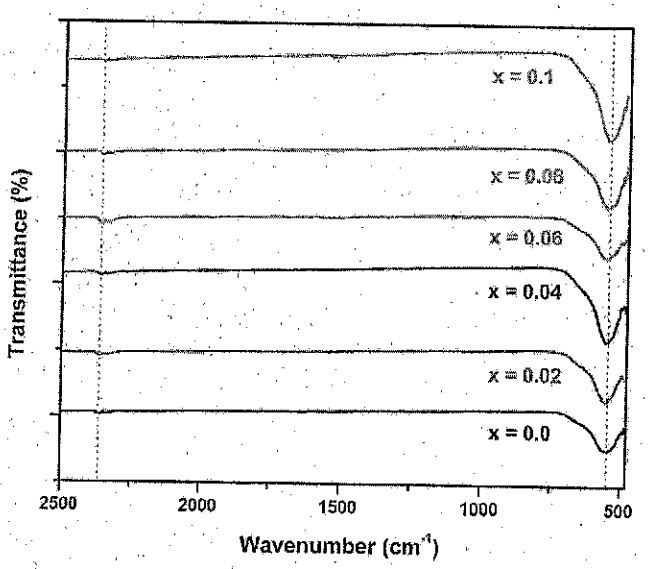

Fig. 8. FT-IR spectra of $CoFe_{2-x}Gd_xO_4$ (x = 0.0, 0.02, 0.04, 0.06, 0.08 and 0.1) nanoparticles.

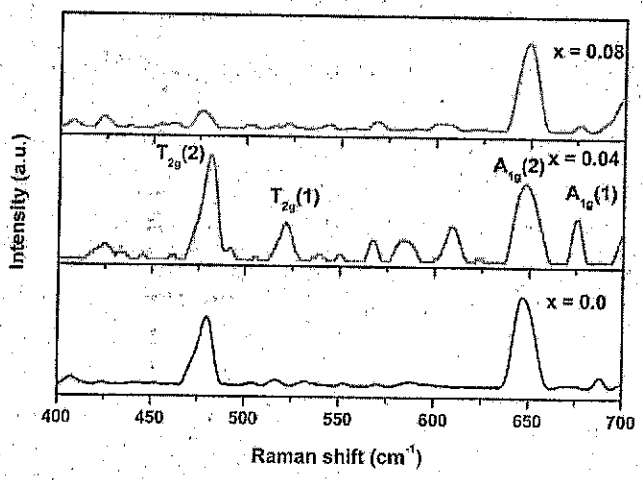

Fig. 9. Raman spectra of $CoFe_{2-x}Gd_xO_4$ (x = 0.0, 0.04 and 0.08) nanoparticles.

Table 5
Raman peaks of $CoFe_{2-x}Gd_xO_4$ (x = 0.0, 0.04 and 0.08) nanoparticles.

Composition (x)	Raman Shift (cm^{-1})			
	$A_{1g}(1)$	$A_{1g}(2)$	$T_{2g}(1)$	$T_{2g}(2)$
0.0	683	647	516	479
0.04	676	648	521	481
0.08	675	649	522	476

these interactions A-B interaction is stronger than the other two interaction [49]. Since the ionic radius of Gd^{3+} ion is greater than other cations in cobalt ferrites, therefore, Gd^{3+} ion is preferred to occupy octahedral [B] sites. At room temperature, Gd^{3+} is non-magnetic; therefore, the number of non-magnetic atoms increases at B-site. Hence, the magnetic moment is decreased at B-site. The resultant magnetic moment is the difference between the magnetic moment at B and A-sites i.e. $M = M_B - M_A$ and consequently reduce the resultant magnetization [50]. Hence, the value of 'Ms' is decreased with Gd^{3+} concentration in cobalt ferrites.

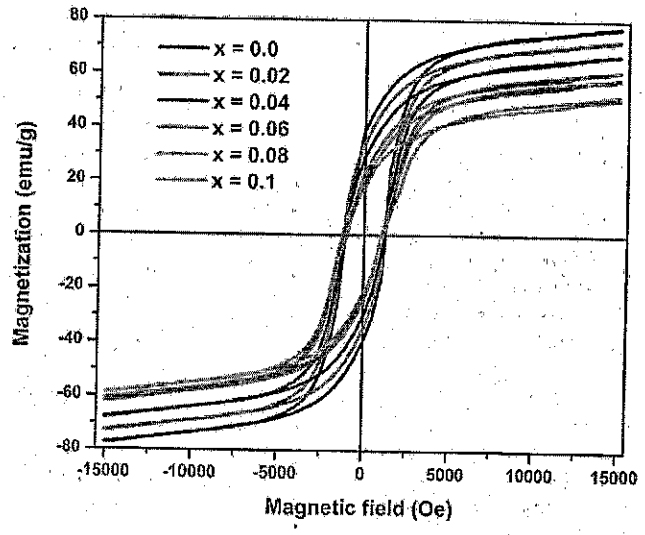

Fig. 10. Magnetic hysteresis loops of $CoFe_{2-x}Gd_xO_4$ nanoparticles.

Table 6
Saturation magnetization (Ms), Coercivity (Hc), Remanence magnetization (R) and observed and calculated magnetic moments (n_BExp and n_BCal.) of $CoFe_{2-x}Gd_xO_4$ (x = 0.0, 0.02, 0.04, 0.06, 0.08 and 0.1) nanoparticles.

Composition (x)	Ms (emu/g)	Hc (Oe)	R	n_B (μ_B)	
				n_BExp.	n_BCal.
0.0	77.37	976	38.99	3.25	4.32
0.02	72.40	1002	34.21	3.07	5.44
0.04	67.05	1087	28.76	2.87	5.60
0.06	61.09	1192	22.61	2.63	5.72
0.08	58.18	1244	19.52	2.53	5.84
0.1	51.38	1281	12.58	2.25	6

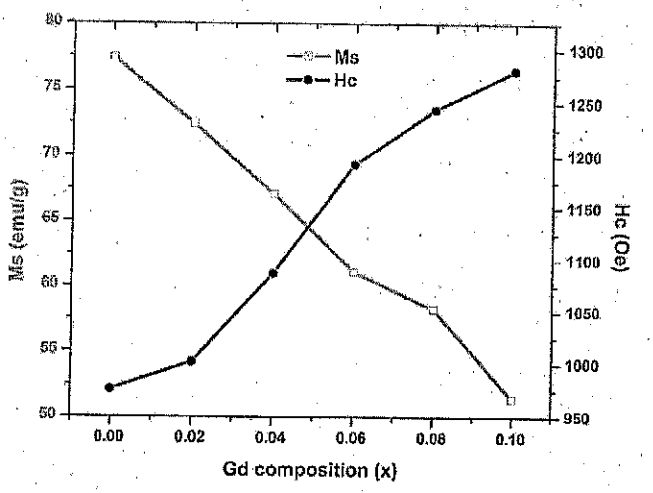

Fig. 11. Variation of saturation magnetization (M_s) and coercivity (H_c) with Gd concentration.

Magnetic properties are collectively depends on grain size, cation distribution, super-exchange interaction, and crystallite size. $CoFe_{2-x}Gd_xO_4$ has the canted magnetic structure for content Fe is less than 2. Fe^{3+} ions occupy both at (A) and [B] site and therefore itinerant electrons can exchange between Fe^{3+} cations. In traditional super-exchange (SE) and double exchange (DE) interaction models,

oxygen anions are assumed to be O^{2-}. It is observed that spinel ferrite also contains negative monovalent oxygen ions; O^{1-} ions (with the electronic configuration $2s^2 2p^5$) [51,52]. This O^{1-} ion can have a 2p hole or 2p electron that affects the magnetic and electric properties through SE and DE models. Since the crystallite size and grain size of samples is decreased with an increase of Gd. The decrease in crystallite size and grain size gives larger dead magnetic area which lowers the magnetization. This result is similar to Nb-substituted cobalt ferrites [53].

From Fig. 11, it is observed that the coercivity of samples is increased from 976 to 1281 Oe with Gd substitution. In general, the coercivity of the samples is inversely proportional to crystallite and grain size. Therefore, the increase of coercivity with Gd-substitution may be due to the decrease of crystallite and grain size. Substitution of Gd could enhance the magnetoelastic and magnetocrystalline anisotropies due to a larger ionic radius and resulting in an increase in 'Hc'. The value of remanence magnetization is decreasing with Gd composition. The experimental value of Bohr magneton number 'n_B' of the samples is determined using the value of 'M_s' from the relation [54]:

$$n_B = \frac{M_W X M_S}{5585} \tag{20}$$

Where M_W is molecular weight and 5585 is the magnetic factor. It is observed from Table 6, that the value of Bohr magneton number decreases from 3.25 to 2.25 with the increase in Gd composition from x = 0.0 to x = 0.1. This is might be due to the decrease in A-B super-exchange magnetic interaction. The magnetic moment per formula unit (n_B) based on Neel's two sub-lattice model were calculated by equation, $n_B = M_B - M_A$, where, M_A and M_B are the magnetic moments (A) and [B] site sub-lattices. The ionic magnetic moments of Co^{2+}, Fe^{3+}, and Gd^{3+} are 3 μ_B, 5 μ_B, and 7 μ_B respectively. The values of calculated magneton numbers are tabulated in Table 6. It is observed that the experimental values of the magneton number are disagreement with Neel's magnetic moment. This is due to the canted magnetic moment and presence of a canted spin structure at octahedral [B] site [55].

3.6. Dielectric properties

The sample powder of $CoFe_{2-x}Gd_xO_4$ (x = 0.0, 0.02, 0.04, 0.06, 0.08 and 0.1) were pressed uniaxial to obtain pellets of diameter 10 mm and thickness 4 mm. The surfaces of pellets were coated for good Ohmic contact. Values of dielectric constant with applied frequency are calculated from the formula [56]:

$$\varepsilon' = \frac{cd}{\varepsilon_0 A} \tag{21}$$

Where C is capacitance, d is the thickness of pellet, ε' is the permittivity of the free space, and A is the cross-sectional area of the pellet. Fig. 12 shows the variation of dielectric constant with applied frequency for all the composition of Gd. It is observed that dielectric constant decreases with applied frequency and shows dispersion at a lower frequency. This might be due to the process of polarization in cobalt ferrite like that of the conducting process. It is found that the process of polarization decreases with frequency and becomes constant at a higher frequency. Above certain higher frequency, the exchange of electron between ferrous and ferric ion does not follow the AC field. The decrease of dielectric constant with the increase of frequency might be due to the interfacial polarization explained by Maxwell-Wagner [57,58]. According to the Maxwell-Wagner model, ferrites are made up of two conducting layers. The larger number of grains occurs in the first layer and the

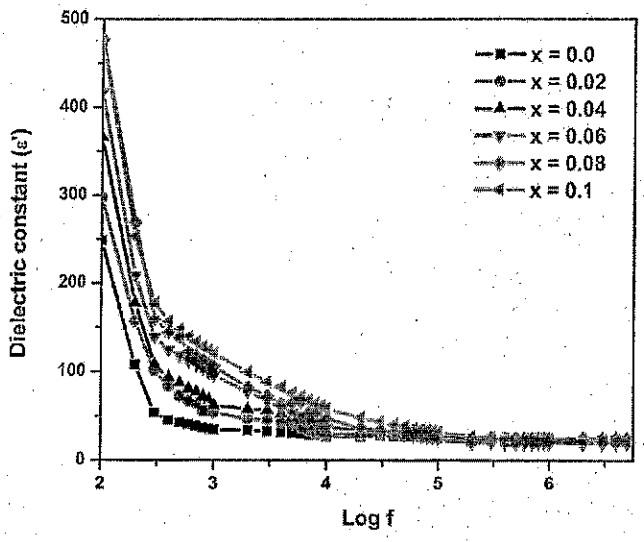

Fig. 12. Variation of dielectric constant with applied frequency of $CoFe_{2-x}Gd_xO_4$.

second layer behaves as poor conductor. These grain boundaries are more effective at lower frequency and therefore value of dielectric constant is high at lower frequency. Grain boundary becomes dominant at higher frequency due to this value dielectric constant is low at higher frequency. In ferrite samples, hopping of electrons takes place following ions,

$$Fe^{3+} + e^- \leftrightarrow Fe^{2+} Gd^{3+} + e^- \leftrightarrow Gd^{2+}$$

$$Co^{3+} + e^- \leftrightarrow Co^{2+}$$

It is observed that the substitution of Gd in cobalt ferrites decreases the value of dielectric constant. At 100 Hz, dielectric constant increases from 248 to 475 with increasing Gd composition from x = 0.0 to x = 0.1. Substitutions of Gd distort the lattice of cobalt ferrite and Co^{2+} ions move towards the tetrahedral site. At the same time, an equal number of Fe^{3+} moves from tetrahedral to octahedral site and exchange of electron between ferrous and ferric ions increases which increase dielectric constant. A similar result is observed in previous literature for Gd-substituted cobalt ferrites [21].

4. Conclusions

The nanocrystalline Gd-substituted cobalt ferrites have been prepared successfully by the technique of sol-gel auto-combustion. Planes in XRD and Rietveld XRD exhibit the evolution of Gd-substituted Co-ferrite with a single phase. It is noticed that the lattice constant decreased with the substitution of Gd composition which reveals that Gd distorts the lattice structure of cobalt ferrites. Values of crystallite and grain size exhibit the formation of nano-crystalline samples. The values of crystallite size and lattice strain estimated from Williamson-Hall effect are decreased with increasing of Gd^{3+} ions in Co-ferrite. The decreasing trend of crystallite and grain size is consistent with magnetic parameters. Rietveld refinement and cation distribution revel that substitution of Gd^{3+} ions in cobalt ferrite is strongly preferred to occupy at octahedral B-site only. The Co^{2+} ions are transferred from octahedral B-site to tetrahedral A-site with the substitution of Gd^{3+} ions by redistributing the cations among the octahedral and tetrahedral site. The presence of the octahedral and tetrahedral bands in FTIR

and Raman spectra also confirmed the phase of spinel ferrite. The band related to spinel ferrite is slightly shifted towards the higher wavenumber which assigned to perturbation occurring between metal-oxygen bond due to the substitution of Gd in Co-ferrite. Values of saturation magnetization, remanence magnetization, and Bohr magneton number are decreased with the increase of Gd composition in cobalt ferrites due to the weakening of A-B super-exchange interaction with Gd^{3+} ions. The values of coercivity increase with Gd composition due to the crystallographic anisotropy with Gd composition. All the samples of Gd-substituted cobalt ferrite follow the Maxwell–Wagner model. Dielectric constant increase with increasing Gd composition is attributed to an increase of densification and transformation of some Fe^{3+} ions. Samples exhibit excellent properties like high crystallization, moderate soft magnetic behavior, and dielectric properties which have promising applications for magneto-optical, communication, and microwave devices.

Declaration of competing interest

The authors declare that they have no known competing financial interests or personal relationships that could have appeared to influence the work reported in this paper.

CRediT authorship contribution statement

A.B. Kadam: Writing - original draft, Investigation, Supervision. **Vishwanath K. Mande:** Writing - original draft. **S.B. Kadam:** Writing - original draft. **R.H. Kadam:** Writing - original draft. **Sagar E. Shirsath:** Investigation, Supervision, Writing - original draft. **Rameshwar B. Borade:** Investigation, Supervision, Writing - original draft.

Acknowledgment

This study was supported by the Dr. Babasaheb Ambedkar Marathwada University, Aurangabad, MS, India. Minor Research Project (Ref: No. STAT/VI/RG/Dept/2018-19/2824-25).

References

[1] M.A. Almessiere, Y. Slimani, A.D. Korkmaz, S. Guner, M. Sertkol, S.E. Shirsath, A. Baykal, Structural, optical and magnetic properties of Tm^{3+} substituted cobalt spinel ferrites synthesized via sonochemical approach, Ultrason. Sonochem. 54 (2019) 1–10.

[2] S.E. Shirsath, D. Wang, S.S. Jadhav, M.L. Mane, S. Li, Ferrites obtained by sol-gel method, in: L. Klein, M. Aparicio, A. Jitianu (Eds.), Handbook of Sol-Gel Science and Technology, Springer, Cham, 2018, pp. 695–735.

[3] M.Y. Chen, J. Xu, Z.Z. Li, Y. Zhang, W.H. Qi, G.D. Tang, Magnetic property and cation distributions in boron-doped MFe_2O_4 (M=Ni, Mn) spinel ferrites, Results Phys 14 (2019) 102389.

[4] M.L. Aparna, A. Nirmala Grace, P. Sathyanarayanan, Niroj Kumar Sahu, A comparative study on the supercapacitive behaviour of solvothermally prepared metal ferrite (MFe_2O_4, M = Fe, Co, Ni, Mn, Cu, Zn) nanoassemblies, J. Alloys Compd. 745 (2018) 385–395.

[5] K.V. Zipare, S.S. Bandgar, G.S. Shahane, Effect of Dy-substitution on structural and magnetic properties of Mn-Zn ferrite nanoparticles, J. Rare Earths 36 (2018) 86–94.

[6] Ru Zhang, Li Sun, Zhenduo Wang, Wentao Hao, Ensi Cao, Yongjia Zhang, Dielectric and magnetic properties of $CoFe_2O_4$ prepared by sol-gel auto-combustion method, Mater. Res. Bull. 98 (2018) 133–138.

[7] S.M. Ansari, S.R. Suryawanshi, M.A. More, Debasis Sen, Y.D. Kolekar, C.V. Ramana, Field emission properties of nano-structured cobalt ferrite ($CoFe_2O_4$) synthesized by low-temperature chemical method, Chem. Phys. Lett. 701 (2018) 151–156.

[8] P.N. Anantharamaiah, P.A. Joy, Tuning of the magnetostrictive properties of cobalt ferrite by forced distribution of substituted divalent metal ions at different crystallographic sites, J. Appl. Phys. 121 (2017), 093904.

[9] M. Cernea, P. Galizia, I. Ciuchi, G. Aldica, V. Mihalache, L. Diamandescu, C. Galassi, $CoFe_2O_4$ magnetic ceramic derived from gel and densified by spark plasma sintering, J. Alloys Compd. 656 (2016) 854–862.

[10] B. Jansi Rani, M. Ravina, B. Saravanakumar, G. Ravi, V. Ganesh, S. Ravichandran, R. Yuvakkumar, Ferrimagnetism in cobalt ferrite ($CoFe_2O_4$) nanoparticles, Nano-Struct. Nano-Objects 14 (2018) 84–91.

[11] G. Datt, M.S. Bishwas, M.M. Raja, A.C. Abhyankar, Observation of magnetic anomalies in one-step solvothermally synthesized nickel–cobalt ferrite nanoparticles, Nanoscale 8 (2016) 5200–5213.

[12] Zein K. Heiba, Mohamed Bakr Mohamed, S.I. Ahmed, Cation distribution correlated with magnetic properties of cobalt ferrite nanoparticles defective by vanadium doping, J. Magn. Magn Mater. 441 (2017) 409–416.

[13] S.S. Desai, S.M. Patange, A.D. Patil, S.K. Gore, S.S. Jadhav, Effects of Zn^{2+}-Zr^{4+} ions on the structural, mechanical, electrical, and optical properties of cobalt ferrites synthesized via the sol–gel route, J. Phys. Chem. Solid. 133 (2019) 171–177.

[14] P.T. Phong, P.H. Nam, N.X. Phuc, B.T. Huy, L.T. Lu, D.H. Manh, In-Ja Lee, Effect of zinc concentration on the structural, optical, and magnetic properties of mixed Co-Zn ferrites nanoparticles synthesized by low-temperature hydrothermal method, Metall. Mater. Trans. 50 (2019) 1571–1581.

[15] S.E. Shirsath, X. Liu, M.H.N. Assadi, A. Younis, Y. Yasukawa, S.K. Karan, J. Zhang, J. Kim, D. Wang, A. Morisako, Y. Yamauchi, Sean Li, Au quantum dots engineered room temperature crystallization and magnetic anisotropy in $CoFe_2O_4$ thin films, Nanoscale Horiz 4 (2019) 434–444.

[16] Y. Sun, Y. Diao, H. Wang, G. Chen, M. Zhang, M. Guo, Synthesis, structure and magnetic properties of spinel ferrite (Ni, Cu, Co)Fe_2O_4 from low nickel matte, Ceram. Int. 43 (2017) 16474–16481.

[17] K. Maaz, S. Karim, A. Mumtaz, S.K. Hasanain, J. Liu, J.L. Duan, Synthesis and magnetic characterization of nickel ferrite nanoparticles prepared by co-precipitation route, J. Magn. Magn Mater. 321 (2009) 1838–1842.

[18] S.R. Wadgane, S.T. Alone, Asif Karim, Gaurav Vats, S.E. Shirsath, R.H. Kadam, Magnetic field induced polarization and magnetoelectric effect in $Na_{0.5}Bi_{0.5}TiO_3$–$Co_{0.75}Zn_{0.25}Cr_{0.2}Fe_{1.8}O_4$ multiferroic composite, J. Magn. Magn Mater. 471 (2019) 388–393.

[19] S.M. Hashemi, S. Hasani, K.J. Ardakani, F. Davarc, The effect of simultaneous addition of ethylene glycol and agarose on the structural and magnetic properties of $CoFe_2O_4$ nanoparticles prepared by the sol-gel auto-combustion method, J. Magn. Magn Mater. 492 (2019) 165714.

[20] Manisha Dhiman, Sonal Singhal, Enhanced catalytic properties of rare-earth substituted cobalt ferrites fabricated by sol-gel auto-combustion route, Mater. Today Proceedings 14 (2019) 435–444.

[21] C. Murugesan, G. Chandrasekaran, Impact of Gd^{3+} substitution on the structural, magnetic and electrical properties of cobalt ferrite nanoparticles, RSC Adv. 5 (2015) 73714–73725.

[22] F.R. Mariosi, J. Venturini, A. da C. Viegasc, C.P. Bergmann, Lanthanum-doped spinel cobalt ferrite ($CoFe_2O_4$) nanoparticles for environmental applications, Ceram. Int. 46 (2020) 2772–2779.

[23] Vinod Tukaram, S.S. Shinde, R.B. Borade, A.B. Kadam, Study of cation distribution, structural and electrical properties of Al–Zn substituted Ni–Co ferrite, Physica B 577 (2020) 411783.

[24] A. Tijerina-Rosaa, J.M. Greneche, A.F. Fuentes, J. Rodriguez-Hernandez, J.L. Menéndez, F.J. Rodríguez-González, Sagrario M. Montemayor, Partial substitution of cobalt by rare-earths (Gd or Sm) in cobalt ferrite: effect on its microstructure and magnetic properties, Ceram. Inter. 45 (2019) 22920–22929.

[25] G.D. Tang, Z.F. Shang, X.Y. Zhang, J. Xu, Z.Z. Li, C.M. Zhen, W.H. Qi, L.L. Lang, Evidence from infrared spectra for the magnetic moment directions of CR cations in the spinel ferrites, Physica B 463 (2015) 26–29.

[26] R.D. Shannon, Revised effective ionic radii and systematic studies of interatomic distances in halides and chalcogenides, Acta Crystallogr. 32 (1976) 751–767.

[27] R.S. Yadav, Ivo Kuřitka, Jarmila Vilcakova, Jaromir Havlica, Lukas Kalina, Pavel Urbánek, Michal Machovsky, David Skoda, Milan Masař, Holek Martin, Sonochemical synthesis of Gd^{3+} doped $CoFe_2O_4$ spinel ferrite nanoparticles and its physical properties, Ultrason. Sonochem. 40 (2018) 773–783.

[28] Rameshwar B. Borade, S.B. Kadam, D.S. Wagare, R.H. Kadam, S.E. Shirsath, S.R. Nimbore, A.B. Kadam, Fabrication of Bi^{3+} substituted yttrium aluminum iron garnet (YAIG) nanoparticles and their structural, magnetic, optical and electrical investigations, J. Mater. Sci. Mater. Electron. 30 (2019) 19782–19791.

[29] A. Ashok, L. John Kennedy, J. Judith Vijaya, Structural, optical and magnetic properties of $Zn_{1-x}Mn_xFe_2O_4$ ($0 \leq x \leq 0.5$) spinel nano particles for trans-esterification of used cooking oil, J. Alloys Compd. 780 (2019) 816–828.

[30] Rameshwar B. Borade, S.E. Shirsath, Gaurav Vats, Anil S. Gaikwad, S.M. Patange, S.B. Kadam, R.H. Kadam, A.B. Kadam, Polycrystalline to preferred-(100) single crystal texture phase transformation of yttrium iron garnet nanoparticles, Nanoscale Adv 1 (2019) 403–413.

[31] R. Jabbar, S.H. Sabeeh, A.M. Hameed, Structural, dielectric and magnetic properties of Mn^{+2} doped cobalt ferrite nanoparticles, J. Magn. Magn Mater. 494 (2020) 165726.

[32] Seema Joshi, Manoj Kumar, Sandeep Chhoker, Arun Kumar, Mahavir Singh, Effect of Gd^{3+} substitution on structural, magnetic, dielectric and optical properties of nanocrystalline $CoFe_2O_4$, J. Magn. Magn Mater. 426 (2017) 252–263.

[33] A. Yazdani, M.R. Jalilian Nosrati, R. Ghasemi, A new approach to spinel ferrites through mean field approximation, J. Magn. Magn Mater. 304 (2006) 433–435.

[34] J. Yan, J. Huang, T. Zhang, H. Tian, J. Yu, L. Zhang, Y. Zhang, Investigation of the microstructure, cation distribution and optical properties of nanoscale

$Ni_xMg_{1-x}Al_2O_4$ spinel pigments, Ceram. Int. 45 (2019) 14073–14083.
[35] Sami ullah Rather, O.M. Lemine, Effect of Al doping in zinc ferrite nanoparticles and their structural and magnetic properties, J. Alloys Compd. 812 (2020) 152058.
[36] W. Qin, T. Nagase, Y. Umakoshi, J.A. Szpunar, Relationship between microstrain and lattice parameter change in nanocrystalline materials, Phil. Mag. Lett. 88 (2008) 169–179.
[37] Y. Slimani, M.A. Almessiere, M. Sertkol, S.E. Shirsath, A. Baykal, M. Nawaze, S. Akhtar, B. Ozcelik, I. Ercan, Structural, magnetic, optical properties and cation distribution of nanosized $Ni_{0.2}Cu_{0.3}Zn_{0.4}Tm_xFe_{2-x}O_4$ ($0.0 \leq x \leq 0.10$) spinel ferrites synthesized by ultrasound irradiation, Ultrason. Sonochem. 57 (2019) 203–211.
[38] S.M. Patange · Sagar E. Shirsath, B.G. Toksha, S.S. Jadhav, S.J. Shukla, K.M. Jadhav, Cation distribution by Rietveld, spectral and magnetic studies of chromium-substituted nickel ferrites, Appl. Phys. A 95 (2009) 429–434.
[39] S.E. Shirsath, M.L. Mane, Y. Yasukawa, X. Liu, A. Morisakoa, Self-ignited high temperature synthesis and enhanced super-exchange interactions of Ho^{3+}–Mn^{2+}–Fe^{3+}–O^{2-} ferromagnetic nanoparticles, Phys. Chem. Chem. Phys. 16 (2014) 2347–2357.
[40] Sonal Singhal, Kailash Chandra, Cation distribution and magnetic properties in chromium-substituted nickel ferrites prepared using aerosol route, J. Solid State Chem. 180 (2007), 396–300.
[41] B.D. Cullity, Elements of X-Ray Diffraction, second ed., Addison Wesley, New York, 1978.
[42] Tahmineh Sodaee, Ali Ghasemi, Reza Shoja Razavi, Cation distribution and microwave absorptive behavior of gadolinium substituted cobalt ferrite ceramics, J. Alloys Compd. 706 (2017) 133–146.
[43] Syed Ismail Ahmad, Shakeel Ahmed Ansari, D. Ravi Kumar, Structural, morphological, magnetic properties and cation distribution of Ce and Sm co-substituted nano crystalline cobalt ferrite, Mater. Chem. Phys. 708 (2018) 248–257.
[44] M. Yehia Mohamed Bakr Mohamed, Cation distribution and magnetic properties of nanocrystalline Gallium substituted Cobalt ferrite, J. Alloys Compd. 615 (2014) 181–187.
[45] L. Krutika, Routray, Sunirmal Saha, Dhrubananda Behera, Rare-earth (La^{3+}) substitution induced changes in the structural, dielectric and magnetic properties of nano-$CoFe_2O_4$ for high-frequency and magneto-recording devices, Appl. Phys. A 125 (2019) 328.
[46] Mohammed S. Al Maashani, Kadhim A. Khalaf, Abbasher M. Gismelseed, Imaddin A. Al-Omari, The structural and magnetic properties of the nano-CoFe2O4 ferrite prepared by solgel auto-combustion technique, J. Alloys Compd. 817 (2020) 152786.
[47] Asima Anwar, Sonia Zulfiqar, , Muhammad Asif Yousuf, Sameh A. Ragab, Muhammad Azhar Khan, Imran Shakir, Muhammad Farooq Warsi, Impact of rare earth Dy^{+3} cations on the variousparameters of nanocrystalline nickel spinel ferrite, J Mater Res Technol (2020), https://doi.org/10.1016/j.jmrt.2020.03.057.
[48] Pradeep Chavan, L.R. Naik, P.B. Belavi, G.N. Chavan, R.K. Kotnala, Synthesis of Bi^{3+} substituted Ni-Cu ferrites and study of structural, electrical and magnetic properties, J. Alloys Compd. 694 (2017) 607–612.
[49] L. Kumar, P. Kumar, V. Kuncser, S. Greculeasa, B. Sahoo, M. Kar, Strain induced magnetism and superexchange interaction in Cr substituted nanocrystalline cobalt ferrite, Mater. Chem. Phys. 211 (2018) 54–64.
[50] B.M. Sahanashree, E. Melagiriyappa, M. Veena, G.J. Shankaramurthy, Influence of Neodymium and gamma rays irradiation on structural electrical and magnetic properties of Co-Zn nanoferrites, Mater. Chem. Phys. 214 (2018) 143–153.
[51] G.D. Tang, Z.Z. Li, L. Ma, W.H. Qi, L.Q. Wu, X.S. Ge, G.H. Wu, F.X. Hu, Three models of magnetic ordering in typical magnetic materials, Phys. Rep. 758 (2018) 1–56.
[52] L.L. Ding, L.Q. Wu, X.S. Ge, Y.N. Du, J.J. Qian, G.D. Tang, W. Zhong, Study of average valence and valence electron distribution of several oxides using X-ray photoelectron spectra, Results Phys 9 (2018) 866–870.
[53] M. Almessiere, Y. Slimani, S. Güner, M. Nawaz, A. Baykal, F. Aldakheel, S. Akhtar, I. Ercan, İ. Belenli, B. Özçelik, Magnetic and structural characterization of Nb^{3+}- substituted $CoFe_2O_4$ nanoparticles, Ceram. Int. 45 (2019), 8222-5232.
[54] S.E. Shirsath, S.S. Jadhav, B. Toksha, S. Patange, K. Jadhav, Influence of Ce^{4+} ions on the structural and magnetic properties of $NiFe_2O_4$, J. Appl. Phys. 110 (2011), 013914.
[55] D.S. Nikam, S.V. Jadhav, V.M. Khot, R.A. Bohara, C.K. Hong, S.S. Mali, S.H. Pawar, Cation distribution, structural, morphological and magnetic properties of $Co_{1-x}Zn_xFe_2O_4$ ($x = 0–1$) nanoparticles, RSC Adv. 5 (2015) 2338–2345.
[56] W.R. Agami, Effect of neodymium substitution on the electric and dielectric properties of Mn-Ni-Zn ferrite, Physica B 534 (2018) 17–21.
[57] R.H. Kadam, K. Desai, V.S. Shinde, Mohd Hashim, S.E. Shirsath, Influence of Cd^{3+} ion substitution on the $MnCrFeO_4$ for their nanoparticle shape formation and magnetic properties, J. Alloys Compd. 657 (2016) 487–494.
[58] M. Hashim, M. Raghasudha, S.S. Meena, J. Shah, S.E. Shirsath, S. Kumar, D. Ravinder, Pramod Bhatt, Alimuddin, Ravi Kumar, R.K. Kotnala, Influence of rare earth ion doping (Ce and Dy) on electrical and magnetic properties of cobalt ferrites, J. Magn. Magn Mater. 449 (2018) 319–327.